Tumor Invasion Margin on the Riemannian Space of Brain Fibers

Parisa Mosayebi, Dana Cobzas, Albert Murtha, Martin Jagersand

University of Alberta

Abstract

Glioma is one of the most challenging types of brain tumors to treat or control locally. One of the main problems is to determine which areas of the apparently normal brain contain glioma cells, as gliomas are known to infiltrate several centimetres beyond the clinically apparent lesion that is visualized on standard Computed Tomography scans (CT) or Magnetic Resonance Images (MRI). To ensure that radiation treatment encompasses the whole tumor, including the cancerous cells not revealed by MRI, doctors treat the volume of brain that extends 2 cm out from the margin of the visible tumor. This approach does not consider varying tumor-growth dynamics in different brain tissues, thus it may result in killing some healthy cells while leaving cancerous cells alive in the other areas. These cells may cause recurrence of the tumor later in time, which limits the effectiveness of the therapy.

Knowing that glioma cells preferentially spread along nerve fibers, we propose the use of a geodesic distance on the Riemannian manifold of brain diffusion tensors to replace the Euclidean distance used in the clinical practice and to correctly identify the tumor invasion margin. This mathematical model results in a first-order Partial Differential Equation (PDE) that can be numerically solved in a stable and consistent way. To compute the geodesic distance, we use actual Diffusion Weighted Imaging (DWI) data from 11 patients with glioma and compare our predicted infiltration distance map with actual grwoth in follow-up MRI scans. Results show improvement in predicting the invasion margin when using the geodesic distance as opposed to the 2 cm conventional Euclidean distance.

Keywords:
Tumor Growth Models, Brain Tumor Invasion Margin, DTI, Riemannian Manifold

1. Introduction

Primary brain tumors are those which start from a glial cell in the nervous system. High-grade variations of these tumors grow very fast, always leading to a life-threatening condition and low two-year survival rate. Although magnetic resonance imaging (MRI) is the imaging mode of choice for the assessment and treatment planning of brain tumors, it is known that conventional MR imaging cannot show tumor infiltration (low concentration of glioma cells).

Infiltrating glioma cells extend beyond the visible enhancement of both T1-weighted and T2-weighted images [1]. Current clinical practice is to segment visible tumor using T2-weighted image, then add an additional 2cm margin uniformly into apparently normal brain to form the treatment volume. This treatment volume receives post surgery radiotherapy in time. However this defined volume is a gross approximation, and for small tumors the treatment volume can often be 4 times larger than the visible tumor volume, potentially sacrificing much healthy brain and unnecessarily degrading brain function and post treatment life quality. The 2cm margin is motivated by biopsies and autopsies on a small population [2], then generalized to all patients.

To improve the therapeutic outcome, more accurate prediction of the tumor invasion margin is necessary. Based on the generally accepted belief that glioma cells preferentially spread along nerve fibers [3], we propose a new (geodesic) distance measure that is not the usual (Euclidean) distance measures in pixels or mm but a distance in curved (Riemannian) space relevant to the likelihood of cancer invasion. This formulation is easily transferable to radiation therapy software by replacing the Euclidean distance currently used to define the 2 cm invasion margin with the new geodesic distance. Moreover, the geodesic model is simple enough (having only one parameter that is kept constant) to be easily tuned to work in a real setting. Instead of continuing to the trend of increasing the model complexity with more parameters, we focus on clinical applicability and validation of our model on real clinical data. This is different in nature, from the previous related work that model the tumor growth. To locate our model among related works and elaborate more on the differences, we provide a brief history of similar and related works.

Many efforts have been made to mathematically model the glioma tumor growth. Following [4], these approaches are classified based on the scale of the observation into two major categories, *Microscopic* and *Macroscopic*. Microscopic models describe the growth process at the cellular level, concentrating on activities that happen inside the tumor cell. They focus on observations coming from *in-vitro* and *in-vivo* experiments. Also, they describe the interactions between tumor cells and their surrounding tissue, the complicated chemical networks inside the tumor cells and also nutrition and oxygen availability. Macroscopic methods, on the other hand, formulate tumor growth in a clinically observable scale, as seen in medical images at millimeter resolution. The images currently used in mathematical modeling include CT scans, MRI and DWI. The only information that is currently extracted from large-scale observations is very limited, including only the tumor delineation area and brain deformation. Limited observations reduce the number of factors included in the modeling, which result in a simpler formulation compared to the microscopic case. Moreover, in contrast to microscopic models that focus on theoretical aspects, macroscopic modeling research is driven by real clinical data, e.g. real boundaries of the brain, tumor region resection and brain tissue characteristics. Hence, evaluation of these models can be done using real patient data. For example, we can validate the growth model using a sequence of MRI images obtained over a period of time.

Almost all macroscopic models formulate the growth process based on two fundamental characteristics of tumors: diffusion and proliferation. These two are formulated together as a general equation called the diffusion-reaction formalism. This formalism was introduced by Murray [5] in 1989 and has significant impact in growth modeling. Diffusion illustrates the fact that tumor cells infiltrate into the surrounding brain tissue. Proliferation is a function representing a reactive behaviour that primarily accounts for tumor cell growth and death. Based on the effect of the tumor growth on the brain [6], macroscopic models are classified into two main subclasses, *mechanical* and *diffusive*.

Mechanical models mainly focus on modeling the effect of tumor growth on deformation of the surrounding tissue. This effect is known as a mass effect. These models couple two

distinct formulations, one for growth and one for the mechanical deformation of the brain tissue. Mohamed *et al.* [7] modeled the tissue as an isotropic and homogeneous hyper-elastic material to generate the large deformations. In this model, tumor growth only consists of proliferation with constant mitosis rate, and the mass effect is generated by the expansion of both the tumor and its surrounding edema. Hogea *et al.* [8] reformulated the same model in a general Eulerian framework with a level-set based approach for the evolving tumor. The new formulation had the advantage of using a regular grid and was more efficient. Hogea *et al.* [8] also extended their mechanical formulation based on Eulerian framework [9]. They later used this general framework for patient-specific parameter estimation [10] and also for image registration [11]. Clatz *et al.* [12] combined the proliferation, anisotropic diffusion and mass effect together. In their model, the brain tissue is considered as a visco-elastic material that can be modeled using a static equilibrium equation. Two different mass effects were established in their model, one for the tumor and the other for the edema.

Diffusive Models formulate the invasion of the tumor in the surrounding brain tissue. This group of methods is based on the reaction-diffusion equation, which has the following general format

$$\begin{cases} \frac{\partial u}{\partial t} = \underbrace{\mathrm{div}(\mathbf{D}\nabla u)}_{\text{Diffusion Term}} + \underbrace{f(u)}_{\text{Proliferation Term}} - \underbrace{T(u)}_{\text{Treatment law}} \\ \\ \mathbf{D}\nabla u.\vec{\mathbf{n}}_{\partial\Omega} = 0 \end{cases} \tag{1}$$

where $\mathbf{D}$ is the diffusion tensor and u is the normalized tumor cell density ($u \in [0,1]$). The second row defines the Neumann boundary conditions and $\vec{\mathbf{n}}$ is the normal to the boundary. Ω shows the domain (3D image) and $\partial\Omega$ is its boundary.

We present this family of macroscopic models based on the diffusion tensor used in the diffusion equation that defines the motility direction of the tumor cells. In early research, a mathematical model of glioma growth and diffusion was developed based on the analysis of serial CT scans of a patient with recurrent anaplastic astrocytoma. The developed model was an isotropic diffusion model that allowed tumor cells to diffuse equally in all directions with the same speed for all tissues [13], [14], [15]. Obviously, these models use simple isotropic tensors for the brain. But, the experimental results of Giese *et al.* [16] established that tumor cells move faster in white matter than in gray matter. Swanson *et al.* [17], [18] incorporated this experimental fact into the growth model by multiplying the isotropic diffusion tensors in white matter with a scaling factor. This isotropic model, which always results in spherical cell invasion, cannot simulate the complex finger-like shapes that characterizes high-grade glioma growth.

Extending Swanson's work, Clatz *et al.* [12], Jbabdi *et al.* [19] and recently Konukoglu *et al.* [20, 21] included anisotropy to the invasion mechanism of tumor cells. By adding anisotropy to the numerical simulation of the tumor diffusion process, the "cloudy like" tumor shapes observed in MRI scans is better captured by the model. These models assume that tumor cells move faster in white matter compared to gray matter and also they follow the white matter fiber tracts in the brain. The Tumor Diffusion Tensor (TDT) in these models are formed from water diffusion tensors extracted from DWI data. Diffusion tensors extracted from DWI data form Diffusion Tensor Images (DTI). TDT is computed from DTI with different methods. The underlying idea of all these methods is to assign an isotropic diffusion to the gray matter and an anisotropic diffusion to the white matter, with the greatest diffusion along the main eigenvector of the water diffusion tensor (see Section 2.5 for more details on the construction of TDT).

One main difference between our work and most macroscopic tumor growth models is that

Paper	Model	Goal	Tensor Type	Source of Tensor	Comparison
Swanson [17]	D	SG	IT	N/A	N/A
Jbabdi [19]	D	SG	DT	Healthy Case	Visual Comparison
Clatz [12]	DM	SG	DT	Atlas	1 Patient
Hogea [9]	DM	SG	DT	Atlas	1 Patient
Konukoglu [22]	D	IM	DT	Atlas	Synthetic Data
Konukoglu [20]	D	SG	DT	Real Tensors	2 Patients
Our approach [20]	D	IM	DT	Real Tensors	11 Patients

Table 1: Summary of related methods in brain tumor growth prediction. The Model comparisons are Diffusion (D) and Diffusion + Mass effect (DM). The Goal comparison is between Simulate Growth (SG) and Invasion Margin (IM). The Tensor Type abbreviations are Isotropic Tensor (IT) and Diffusion Tensor (DT). N/A is used when the information is not given.

we directly define the tumor invasion margin, not the tumor growth. Konukoglu *et al.* [22, 21] are among the few who had the same approach in capturing the tumor invasion margin by extrapolating the low tumor densities in MRI images. For extrapolation, they considered the traveling solution of the reaction-diffusion equation in an infinite cylinder. We summarize related macroscopic tumor models in Table 1, providing the comparison between the previous researches and our work.

1.1. The Contributions of This Study

We can summarize the contributions of our study as follows.

1.1.1. DTI-based Geometric Model

This study is the extension of our preliminary study [23], where we introduce a novel model to predict the tumor invasion margin using the geodesic distance defined on the Riemannian manifold of brain diffusion tensors. The formulation of white matter as a Riemannian manifold was first introduced by O'Donnell *et al.* [24] and later formalized by Lenglet *et al.* [25]. Our modified distance model is designed for predicting only the current tumor spread (invasion, not visible in regular MRI) at the time of imaging. The purpose is to better target immediate treatment following the imaging. Our plans are to use it for better radiation therapy planning. Therefore, the diffusion-based geodesic distance model does not include components of a growth model like mass effect or proliferation. The proposed distance formulation is easily transferable into radiation treatment planning software that currently makes use of a distance (Euclidean) in defining the target region, as it predicts the distance occult cells have reached beyond the visible tumor margin. In addition, this formulation results in a first-order PDE that has stable finite differences solutions. However, anisotropic models based on the 2nd order diffusion equation ([19, 12, 21]) cannot be implemented in a stable way using the common basic finite difference schemes in the literature and more complicated methods and careful stability analysis would have to be performed [26].

1.1.2. Test on Real Data

In addition to introducing the geodesic distance as a measure of glioma cell infiltration, another contribution of this study is the validation of our model on actual patient-specific DTI data. A main limitation of the published DTI-based models is the lack of validation with real patient DTI data. We concentrate here on getting a model that best agrees with real data and therefore

can be useful in a clinical setting. Some of the mentioned models use non-patient DTI data, either on atlas tensors registered with the patient (Clatz *et al.* model [12]) or tensors from a single healthy subject that are unregistered with the patient (Jbabdi [19]). Konukoglu *et al.* [22] validate their model by simulating a synthetic tumor on a healthy brain and by comparing the simulation result with the simulation result of another method. Better validation methods compare the visible tumor growth in MR images with the one simulated by the model [20]. However, none of the models are validated on more than two cases.

We tested our model on 11 different patients by comparing the predicted infiltration distance map computed based on an initial DTI scan with real growth shown on later MRI or DTI scans of the same patient. Our method takes into account natural barriers to glioma growth such as the skull, the tentorium cerebelli and the falx cerebri. Comparative results of using geodesic distance show an acceptable improvement vs. uniform (Euclidean) distance.

1.1.3. Relation to existing work
2. Materials and Methods

2.1. Tumor Invasion Using Geodesic Distance on Brain Fiber Manifold

In this section, we introduce a new method that directly calculates the glioma cell infiltration in the format of a distance function from the original visible tumor location. Based on the general belief that that tumor cells infiltrate (diffuse) along white matter fibers [3], the proposed method calculates a geodesic distance on a Riemannian manifold characterized by the anisotropic diffusion operator defined by DTI (Riemannian manifold of of brain fibers).

O'Donnell *et al.* [24] and Lenglet *et al.* [25] introduced the formulation of the white matter as a Riemannian manifold characterized by the infinitesimal anisotropic diffusion operator. They made the link between the diffusion tensor data D and white matter manifold geometry and showed that the diffusion operator can be associated with a metric $G = D^{-1}$. This metric allows computation of geodesic paths and distances between points on the brain, and it was used in [25] to compute fiber connectivity.

To explain this geometric idea, we employ an analogy with city traffic. Using the Euclidean distance for the tumor margin corresponds to the assumption that it takes the same time to drive to any point on a city map at a particular radius from home. However, transport time to a certain point in a city depends to a large extent on the road net geometry and traffic flow. The same is true for glioma spread, which depends on the brain structures in its vicinity. The DTI technique that measures water diffusion in brain tissue gives us the key to design a roadmap of the brain. We make maps that consistently mark every 3D voxel (space unit) in the brain with a modified distance from the current tumor. The mathematically correct way to do this is to compute a geodesic distance on a Riemannian (curved) manifold of brain fibers.

An advantage of this new formulation is that it results in a first order Hamilton-Jacobi equation, while prior works on tumor growth modeling [19, 12, 18] directly solve the second order parabolic diffusion Equation 1. The first order Hamilton-Jacobi has a stable finite difference-based numerical solution. But, solving the second order anisotropic diffusion equation with finite difference method has many stability issues. The stability issues are more difficult to tackle in the 3D case. The numerical aspects are explained in further details in Section 2.6 and Appendix A, while details on the stability of finite difference methods for solving the 2D anisotropic diffusion PDEs are presented by Weickert [27].

2.2. *Geometry of Manifold from Diffusion Processes*

First we define the manifold geometry from the water diffusion process. We represent the motion of water molecules by Brownian motion X_t. Transition mechanisms are determined by a probability density function p or an infinitesimal generator $\mathcal{L}$. The infinitesimal generator characterizes the Brownian motion as a molecular diffusion process.

$$\frac{\partial u}{\partial t} = \text{div}(D\nabla u) = \mathcal{L}u \tag{2}$$

where D is the positive definite order-2 tensor and u is the cell density. Lenglet *et al.* [25] show that under some technical hypothesis on $\mathcal{L}$ and the Brownian motion X_t, it is possible to define an $\mathcal{L}$-diffusion process on a Riemannian Manifold M from the d-dimensional stochastic process X_t. Here we follow their theory on building the connection between the $\mathcal{L}$-diffusion process and the Riemannian Manifold. The main focus is on the case of diffusion processes with a time-independent infinitesimal operator $\mathcal{L}$ that is assumed to be smooth and non-degenerate elliptic. We define the Laplace-Beltrami differential operator for a function f on a Riemannian manifold M,

$$\Delta_M f = \text{div}(\text{grad} f) \tag{3}$$

Denoting the discrete manifold metric $G = \{g_{ij}\}$ with its inverse $\{g^{ij}\}$, the Laplace-Beltrami operator can be written as

$$\Delta_M f = \frac{1}{\sqrt{G}} \frac{\partial}{\partial x_j} \left(\sqrt{G} g^{ij} \frac{\partial f}{\partial x_i} \right) = g^{ij} \frac{\partial^2 f}{\partial x_i \partial x_j} + b^i \frac{\partial f}{\partial x_i} \tag{4}$$

where

$$b^i = \frac{1}{\sqrt{G}} \frac{\partial(\sqrt{G} g^{ij})}{\partial x_i} \tag{5}$$

We can omit the second term of 4, since Δ_M is second order and strictly elliptical.

Definition: The operator $\mathcal{L}$ is said to be an intrinsic Laplacian generating a Brownian motion on M if

$$\mathcal{L} = \frac{1}{2} \Delta_M \tag{6}$$

For a smooth and non-degenerate elliptic differential operator on M, $\mathcal{L}$ is written as

$$\mathcal{L} = \frac{1}{2} d_{ij} \frac{\partial^2}{\partial x_i \partial x_j} \tag{7}$$

where d_{ij} are the components of the diffusion tensor $D = \left\{ d_{ij} \right\}_{i,j=1...d}$. Equations 4, 5 and 7 conclude in the following lemma:

Lemma: If $\left\{ d^{ij} \right\}_{i,j=1...d}$ denotes the inverse matrix of D, then $g = d^{ij} dx_i dx_j$ defines a Riemannian metric g on M.

Conclusion: This ends up in a very important concept in diffusion tensor imaging, that the

diffusion tensor D estimated at each voxel point, after inversion, defines the metric of the manifold. In this way, the link between the diffusion tensor data and the manifold geometry of brain fibers is made.

$$G = D^{-1} \qquad (8)$$

Now that we have the metric of the manifold, we are able to define the tumor invasion margin as the distance from the initial tumor location on the Riemannian Manifold M. The idea is that water molecules starting from a given point x_0 on M can reach to any point x on M through a geodesic under Brownian motion. Here, the geodesic distance between the two points shows the pathway of molecular Brownian motion (along fibers in the brain).

We can compute these geodesics using the metric g of the manifold. Let us define Riemannian distance from a fixed starting point $x_0 \in M$ to another point x on the manifold as $r(x) = \phi(x_0, x)$ where $r : M \rightarrow \Re_+$. Based on [25], under the assumption that M is geodesically complete, there is a unique distance minimizing the geodesic between each two points on the manifold. The distance function is Lipschitz on all M, smooth on M/Cut_{x0} where Cut_{x0} is the location of all the points where the geodesic starting orthonormally from x_0 stops being optimal for the distance. The distance function on M/Cut_{x0} has the property $|\mathrm{grad}\phi(x)| = 1$ where $\mathrm{grad}\phi(x)$ denotes the gradient of the distance function on the tangent plane of the manifold. This results in the general definition of the distance function.

2.3. Geodesic Distance Function

The distance function ϕ from a non-empty closed subset K is the unique viscosity solution of the Hamilton-Jacobi Equation [25]

$$\begin{cases} |\mathrm{grad}\phi| = 1 & \text{in} \quad M \backslash K \\ \phi(x) = \phi_0(x) & \text{for} \quad x \in K \end{cases} \qquad (9)$$

where $\phi_0(x) = 0 \ \forall x \in K$ in the class of bounded uniformly continuous functions. This is a well-known eikonal equation on the Riemannian Manifold (M,g).

The general format of this Hamilton-Jacobi equation with Dirichlet boundary conditions is written as

$$\begin{cases} H(x, D\phi(x)) = 0 & \text{in} \quad M \backslash K \\ \phi(x) = \phi_0(x) & \text{for} \quad x \in K \end{cases} \qquad (10)$$

where the Hamiltonian $H : M \times T^*M \rightarrow \Re$ is a continuous real function on the cotangent space of the manifold (T^*M). Equation 9 is achieved by setting $H(x, D\phi(x)) = |\mathrm{grad}(\phi(x))| - 1$ in 10. We denote by $|v|$ the magnitude of a vector v of TM (tangent plane of M), defined as $\sqrt{g(v, v)}$. In matrix notation by forming $G = \{g_{ij}\}$ the metric tensor, this writes as $\sqrt{v^T G v}$.

2.3.1. A Level Set Formulation for Distance Function

The viscosity solution ϕ at $x \in M$ of Equation 9 is not a smooth solution. But it has the property that it is the minimum time $t \geq 0$ for any curve γ to reach a point $\gamma(t) \in K$ starting at x with the condition $\gamma(0) = 0$ and $\left|\frac{\partial \gamma}{\partial t}\right| \leq 1$. Based on this fact, Equation 9 can be solved as a dynamic problem and we can apply a level set method for its numerical solution [28].

The level set formulation introduces the use of an implicit function of one higher dimension to solve the dynamic equation. In this way, the problems of instabilities, deformation of surface elements and topological changes are avoided. In the level set formulation, the distance function ϕ is the zero level of an implicit smooth function $\psi(x, t)$ at time t. ϕ is the zero level set which

means the set of points of the manifold that have already been visited. $\psi(x, t)$ is a compact functional of higher dimension, which divides M into $\Gamma \in M$ and its complement $\Gamma^c \in M$. We call Γ the interior part (which means points of the manifold that have already been visited) and Γ^c the exterior (the points not visited). As a result, $\psi(x, t)$ has the following property at $t = 0$

$$\begin{cases} \psi(x, 0) = 0 & \Leftrightarrow x \in \phi_0 \\ \psi(x, 0) > 0 & \forall x \in \Gamma \\ \psi(x, 0) < 0 & \forall x \in \Gamma^c \end{cases} \tag{11}$$

$\psi(x, 0)$ is a uniformly continuous and monotonic strictly decreasing function of distance near ϕ_0. We can initialize ψ with a Euclidean signed distance function. We require ϕ_t to evolve so that:

$$\psi(x, t) = 0 \Leftrightarrow t = \phi(x) \tag{12}$$

The level set generated by Equation 12 is the viscosity solution of 9 if ψ is the viscosity solution of [25]

$$\begin{cases} \psi_t + F(t, x, D\psi(t, x)) = 0 & \forall t > 0 \\ \psi(x, 0) = \psi_0(x) \end{cases} \tag{13}$$

$F > 0$ does not change sign and it is defined as

$$F(t, x, D\psi) = H(t, x, D\psi) + 1 \tag{14}$$

So Equation 13 becomes

$$\begin{cases} \psi_t + |\mathrm{grad}\psi| = 0 & \forall t > 0 \\ \psi(x, 0) = \psi_0(x) \end{cases} \tag{15}$$

where ψ_0 is the signed distance function of ϕ_0. The viscosity solution of this PDE gives us the geodesic distance function as the zero level of ψ in time.

2.4. Geodesic Distance for Tumor Growth Prediction

When using the geodesic distance in the context of growth prediction, the subset K from where we initiate the growth represents the visible tumor margin. In addition, as the brain contains several obvious natural barriers to glioma growth such as the skull, ventricular system, the tentorium cerebelli and the falx cerebri, M is defined as the brain volume that does not contain those barriers.

2.5. Extracting Tumor Diffusion Tensor (TDT) from DTI

Tumors grow with different speed in white vs. gray matter (with a factor of about 10 [17]). While ideally this should be directly reflected by the diffusion tensors (DT) magnitude, due to noise and discretization problems and the fact that the tumor might grow at a different speed as water diffusion, so that $D \neq DT$.

So-far published transformation of DTI data into TDT are rather heuristic [19], [20]. TDT is typically constructed by assigning an isotropic diffusion to the gray matter and an anisotropic diffusion to the white matter, with the greatest diffusion along the main eigenvector of the DT, corresponding to the direction of white matter fibers. In principle, more elaborate models could be developed by estimating better TDT parameters from tumor growth observed in real patient data. For example one could estimate a function $D(x) = C(x)DT(x)$ where $C(x)$ is a spatial transform function. In practice such an approach requires large amounts of patient growth data,

(a) Barriers   (b) Geod. dist.   (c) Geod. dist. on   (d) Geod. dist.
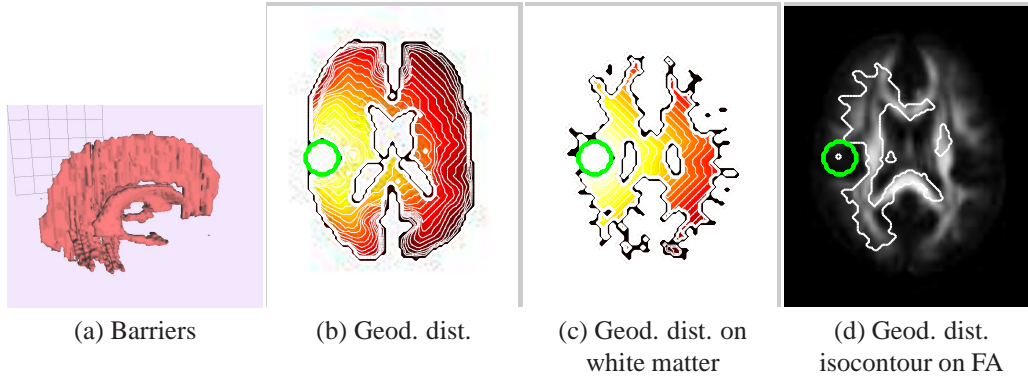white matter   isocontour on FA

Figure 1: The result of applying the geodesic distance model to a DTI atlas. Colors in (b) (c) show the geodesic distance from the initial position (scale: yellow=close, red=far). (d) Shows a 2D cut through an isosurface of the geodesic distance.

a better understanding of what TDT models would be physiologically plausible, and, at the same time, the models should be simple enough to yield a numerically well conditioned estimation problem.

Figure 1(a) shows an example of segmented barriers (ventricles, falx, tentorium). Figure 1(b-d) shows examples of geodesic distance computed on the ICBM DTI-81 atlas [29]: (b) shows the geodesic distance computed with linearly weighting the tensors that originates from a sphere (green circle in the figure) until it reaches the skull boundary; (c) shows the geodesic distance but with thresholding only the white matter tensors instead of scaling the whole brain tensors; (d) shows an isocontour of the geodesic distance aligned with FA values. Notice how the distance follows the fiber directions.

2.6. Numerical Aspects of the Geodesic Model

To numerically solve the hyperbolic Hamilton-Jacobi Equation 15, we approximate the continuous flux $|\text{grad}\psi|^2$ as [25]

$$
|\text{grad}\psi|^2 = \begin{aligned}
&\sum_{i=1}^{3} g^{ii}\left(\max(D_{x_i}^{-}\psi, 0)^2 + \min(D_{x_i}^{+}\psi, 0)^2\right) + \\
&\sum_{i\neq j} g^{ij}\text{minmod}(D_{x_i}^{+}\psi, D_{x_i}^{-}\psi)\text{minmod}(D_{x_j}^{+}\psi, D_{x_j}^{-}\psi)
\end{aligned} \tag{16}
$$

where $g_{i,j=1...3}^{ij}$ are components of the inverse matrix G^{-1}, $D_{x_i}^{\pm}\psi$ are the upwind approximation of the gradient of ψ in x_i and $\text{minmod}(a, b) = \min(a, 0) + \max(b, 0)$. With this approximation of the flux, we used an explicit method to solve Equation 15 on the whole domain, using a fast-marching method for reinitializing the signed distance function [30] after each iteration.

Equation 15 is a Hamilton-Jacobi equation that is a first order hyperbolic (wave-like) PDE of the form $\phi_t + H(\phi_x) = 0$. Hamilton-Jacobi equations are very similar to classical hyperbolic conservative laws [30]. The finite difference method of Equation 16 is spatially stable and its time stability is simply satisfied by adjusting the temporal resolution. Appendix A gives details on the stability and consistency of our solution.
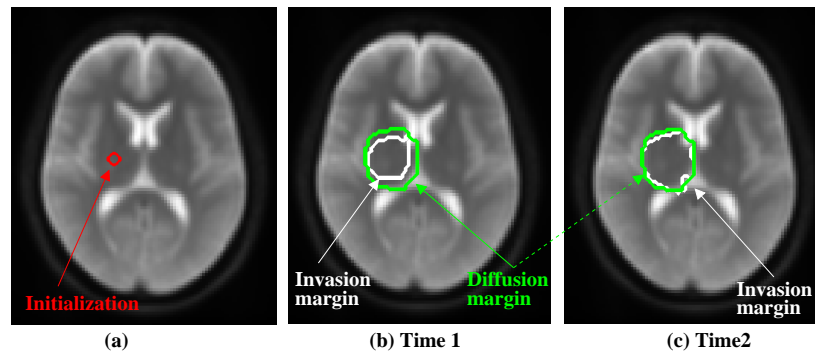
Figure 2: Synthetic diffusion-growth simulation on a DTI atlas to motivate our validation. The experiment shows that the visible tumor margin at later scans (*Time 2*) is close to the actual (invasion) tumor margin in earlier scans (*Time 1*). We set the density of visible cancer cells to 0.05. Synthetic tumor growth is generated from a seed region show in (a) using diffusion. (b) *Time 1*: after simulated growth we show tumor margin - visible in blue (iscontour of density=0.05) and actual in green (isoconour of density 0) (c) *Time 2*: after running diffusion few more iterations the visible margin (isconour of density=0.05) is very close to the actual tumor margin from time1.

3. Experiments

3.1. Validation with Real Data

We have proposed a modified distance to better capture tumor invasion margin by taking into consideration preferential spread along white matter fibers. Unfortunately, we cannot use any direct method to evaluate our mathematical model since the invasion margin is not observable in any of the available imaging techniques. We instead validate our model using subsequent MRI scans that show actual tumor growth (typically 3 month later). Our main assumption is that the visible growth in the subsequent times occurs over the invisible but already-infiltrated regions at the initial time. Figure 2 presents a simple diffusion-based growth simulation that uses Equation 1 to support our assumption. We synthetically generate two stages of growth using anisotropic diffusion in a DTI atlas and show that the visible tumor margin (choosing a threshold of 0.05 for visible cell density) at later scans (*time 2*) is close to the invasion (actual tumor) margin in the earlier scans (*time 1*).

Based on this assumption, we compare the geodesic distance generated from data *time 1* with the segmented visible tumor in the later *time 2* scan. For a fair comparison we calculated the volume change between the segmented tumor in *time 2* and *time 1* and chose the isocontour corresponding to this volume change. We also compared our geodesic model with a uniform Euclidean model where the corresponding isocontour for the Euclidean model was calculated the same way. One challenge in such validation system is that what we see in a later scan is actual growth that includes mass effect and proliferation. We ignore proliferation and account for the mass effect through image registration. We excluded proliferation from our model because the effect of proliferation cannot be isolated from the effect of diffusion [20]. While this is only an approximate validation procedure, it still gives a good indication that our new distance would better predict tumor infiltration than the uniform distance that is currently used in clinical practice.

Fig. 3 shows an overview of our *validation* system, and Fig. 4 pictorially illustrates validation steps. A brief explanation and motivation is provided below and more details in the following subsections.

Validation data To minimize the effect of radiation treatment, we chose the first or second DTI scans after treatment as the *time1* (initial) scan. The *time2* (reference) scan used for comparison is taken as subsequent clinical MRI-FLAIR scan typically after 3 month. While ideally a later DTI scan could have been used for comparison, for most patients, due to their degraded health condition, we do not have a second DTI scan (the DTI study is not part of their clinical scan and therefore not mandatory).

Tumor/edema segmentation The geodesic model is initialized from the visible tumor segmented on *time1* FLAIR image taken at the same time as the DTI scan. The reference tumor used for comparison is segmented in the *time2* FLAIR scan. This segmentation corresponds to the tumor and edema region. We chose to do segmentation on a FLAIR image because there is evidence that occult cells are present at about 2cm distance from edema as visible on a FLAIR/T2 [2]. The FLAIR abnormality is also the reference tumor volume enhanced with a 2m margin that is currently considered for radiation treatment. This *time2* segmentation is used to calculate the volume change that is used to identify the isocontour in the *time1* geodesic distance corresponding to the *time2* visible tumor. To be able to compare the two scans they need to be registered.

Tumor barriers Tumor spread barriers (ventricular system, falx cerebri and tentorium cerebelli), which are also required by the geodesic distance model, are manually delineated in *time1* scan.

Data Registration Registration between *time2* and *time1* need to be performed in order to do the validation. The presence of mass effect between the two scan, would suggest that a non-linear registration should be used to 'undo' this process. Although, we applied different techniques to tackle the mass effect problem with non-linear registration (one method is described in [23]), since the available non-linear registration techniques do not work accurately on images with pathological abnormalities, using non-linear registration did not improve the results. We therefore chose to do a simple linear registration between the two scans.

Measurements We compared the accuracy of the predicted infiltration using the geodesic and Euclidean model with the actual tumor growth from *time2*. Both distances are computed up to the volume change between the two time scans. Since in clinical practice, the 2cm margin does not take into account natural brain barriers we analyzed two cases for the Euclidean distance: with and without barriers. While the first one represents current clinical practice, the later one is a more fair comparison with the geodesic distance that accounts for brain barriers. We report Jaccard scores as results of our comparison in Table 2 and we show visual comparison on selected slices in Figure 6 and Figure 7.

3.2. Patients and Data

We have 64 patients involved in the DTI glioma study[1]. After processing all data we only found 11 patients that were useful for our study (showing tumor growth between the first DTI scan and subsequent scans). The 11 patients included in the validation have mostly 4 grade glioblastoma (8 cases), one has grade 3 glioma and two have grade 2 malignant glioma.

---

[1]The data collection protocol was approved by REB and the patients that have signed and given informed consent.
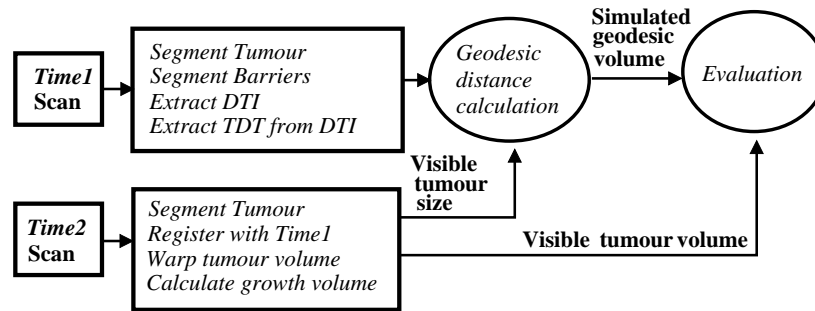
Figure 3: Overview of the tumor growth validation system

DWI images have been acquired on a research-dedicated 3T Philips Achieva located at a local hospital. The relevant DWI acquisition parameters for full brain coverage are: single-shot echo planar imaging with a SENSE factor of 2, 60 2.3 mm thick slices with no gap, field-of-view $= 220 \times 220$ mm^2, 2.3 mm^3 isotropic resolution, echo time $= 88$ ms, repetition time $= 8.8$ s, 2 averages, acquisition time $= 5$ min, diffusion sensitivity $b = 1000$ s/mm^2, and 15 diffusion-sensitizing gradient directions. In addition, a 3-dimensional isotropic T1-weighted image depicting the tumor is also acquired at 3T with $1 \times 1 \times 1$ mm^3 resolution in 5.5 min for anatomical comparison and co-registration with the 1.5T images. Routine MRI scans (T1 pre- and post-contrast, T2, FLAIR) are all acquired on the clinical 1.5T Philips scanner as part of the patient's standard follow-up. The resolution of DWI data is $128 \times 128 \times 60$ and the resolution of FLAIR data is $512 \times 512 \times 21$.

Each patient has a pre-RT (Radiation Therapy) MRI scan. Follow-up DWI or MRI scans have been made after treatment at intervals of about 3-6 months for the duration of life of the patient. Typically at least one or two DWI scans are acquired after radiation and the rest of the scans are conventional MRI images (T2, T1C, FLAIR). After processing all data we only found 11 patients that were useful for our study (showing tumor growth between the first DTI scan and subsequent scans).

3.3. Data processing

3.3.1. Segmentation and Tensor Extraction

For the validation procedure and for initializing the growth simulation, the area of tumor cells visible in the MRI data has to be segmented. The region containing the tumor and its associated edema is the high signal area visible in FLAIR data. We used an a semi-automatic segmentation software that we have developed in our lab [31] to do all segmentations. In addition to the tumor region, growth barriers (ventricular system, falx cerebri and tentorium cerebelli), which are also required by the growth prediction model, are manually delineated using the same software. An expert radiation oncologist validated all segmentations.

We use ExploreDTI [32] as the tensor processing tool to extract the tensor data from 15 diffusion-weighted images on a voxel-by-voxel basis. ExploreDTI has the post processing option for correcting eddy current distortions that are unique for each diffusion-encoding direction and also for correcting the motion distortions. We post-process water tensors (DTI) to make tumor diffusion tensors (TDT) as explained in Section 2 by weighting the tensors based on their Fractional Anisotropy (FA) value.
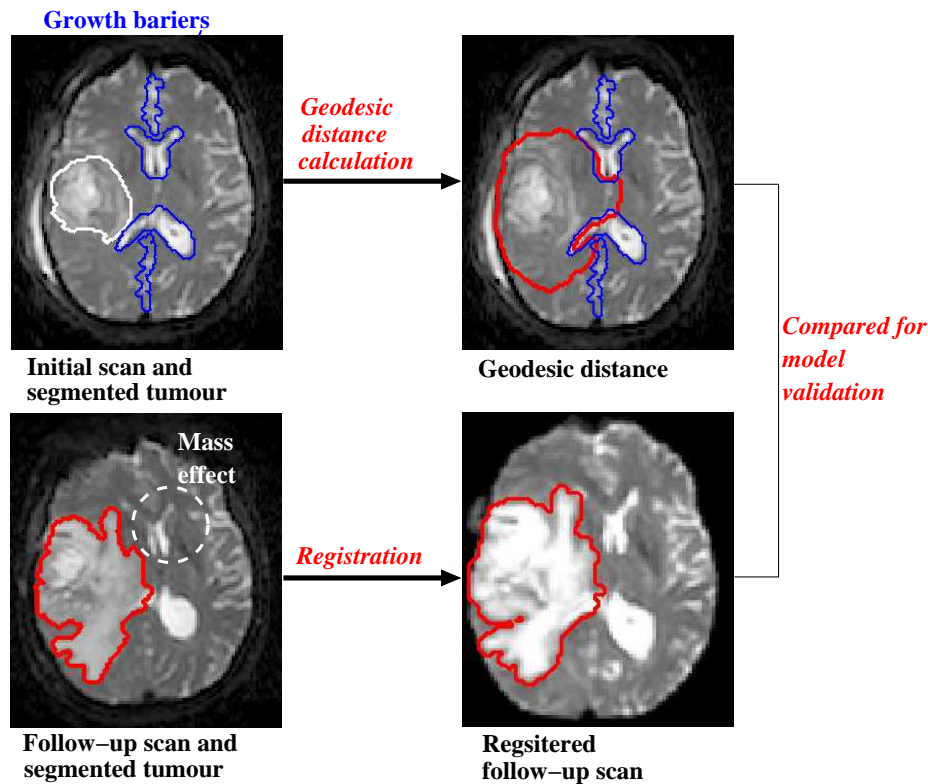
Figure 4: We compute the geodesic distance on *time1* corresponding to the same volume as the growth shown on the registered *time2* scan. Even though this registration does not solve the non-linear effects caused by the mass effect, it is still a good approximate alignment between the two time scans.

3.3.2. Registration

To be able to compare the simulated isocontours with the visible growth observed in a later scan, we need registration.

Our registration includes two steps; registering FLAIR data from *time2* with the FLAIR data from *time1* and also registering the FLAIR and DWI-b0 data of *time1*. For both cases, we use affine (linear) registration. One source of registration errors is the difference in resolution between DWI images ($128 \times 128 \times 60$) with FLAIR images ($256 \times 256 \times 20$). The difference between the inter-slice distances is most notable. As Figure 5 shows a typical result of our registration procedure.

The linear registration does not take into account the mass effect due to the tumor growth from *time1* to *time2*. This is easily noticed in Figure 4 (right-bottom) which shows the result of affine registration: the growth-affected ventricle shape in *time2* is incorrectly registered with data at *time1*. Even though a nonlinear registration would be more suitable to account for the mass-effect, we have found, after applying different methods (one method is described in [23]), that non-linear registration only makes results worse. For accounting the abnormal tissue, we have masked the tumor region in both the target and source images before applying the non-linear registration. Considering this, the abnormal tissue should not interfere with the registration

Initial FLAIR Scan

Initial FLAIR Scan after Interpolation + Registration

Initial DWIb0 Scan

Time2 FLAIR Scan

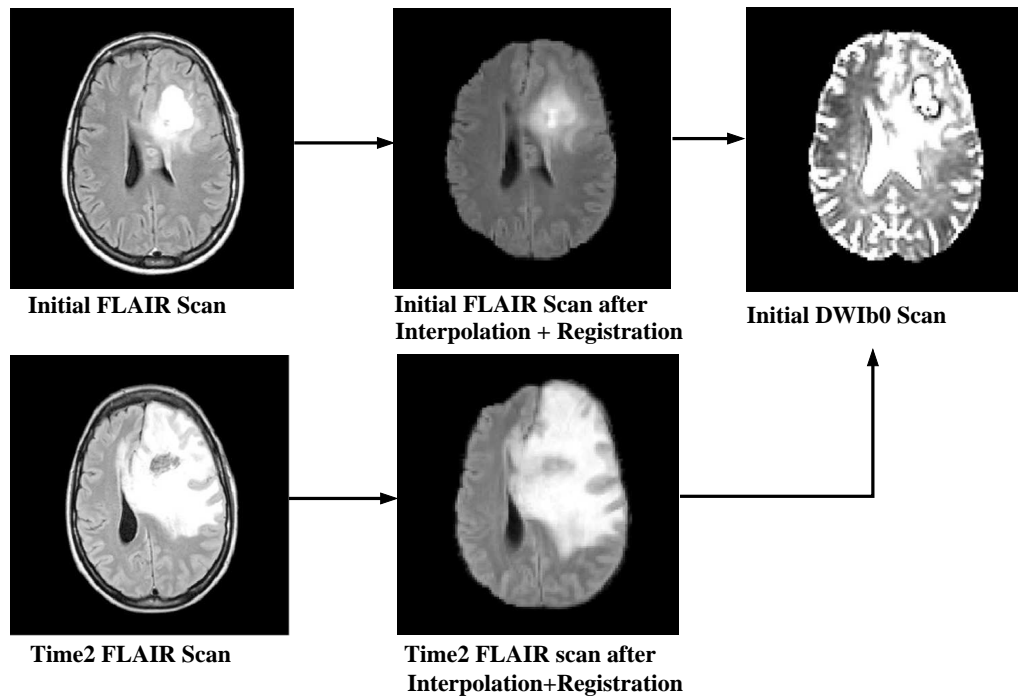**Time2 FLAIR scan after Interpolation+Registration**

Figure 5: The low inter-slice resolution FLAIR images at *time1* and *time2* scans are linearly registered to DWI-b0 at *time1* scan.

process, but still the algorithm was not able to correctly register the two images. The failure of non-linear registration methods is probably due to the fact that available techniques do not work accurately on images with pathological abnormalities and masking the abnormal region is not enough. For both linear and non-linear registrations, we use FSL tools [33] (FLIRT for linear and FNIRT for non-linear registration).

3.4. Results on real DTI for geodesic distance validation

3.4.1. Comparison with the traditional uniform distance model

As a result of our validation procedure for the geodesic distance on real DTI data, we report comparative results between the predicted infiltrations on *time1* scan using the geodesic and Euclidean model with the actual tumor growth from *time2*. Both distances are computed up to the volume change between the two time scans. For the Euclidean distance, we analyze two cases: one that accounts for brain barriers (more fair comparison with the geodesic distance case) and one that does not consider brain barriers (closer to the clinical practice).

Figure 6 presents comparative results between the geodesic distance and the Euclidean distance with no barriers (real clinical practice). We noticed that where the tensor values are less noisy, the geodesic distance model can track the path of fibers, and therefore the model matches tumor growth, as opposed to the Euclidean model. As presented slices are parts of a 3D volume, initial tumor contour is not present in two of the slices (tumor has not reached that slice but it will later grow there). Notice how in the example from the last row of Figure 6 the Euclidean

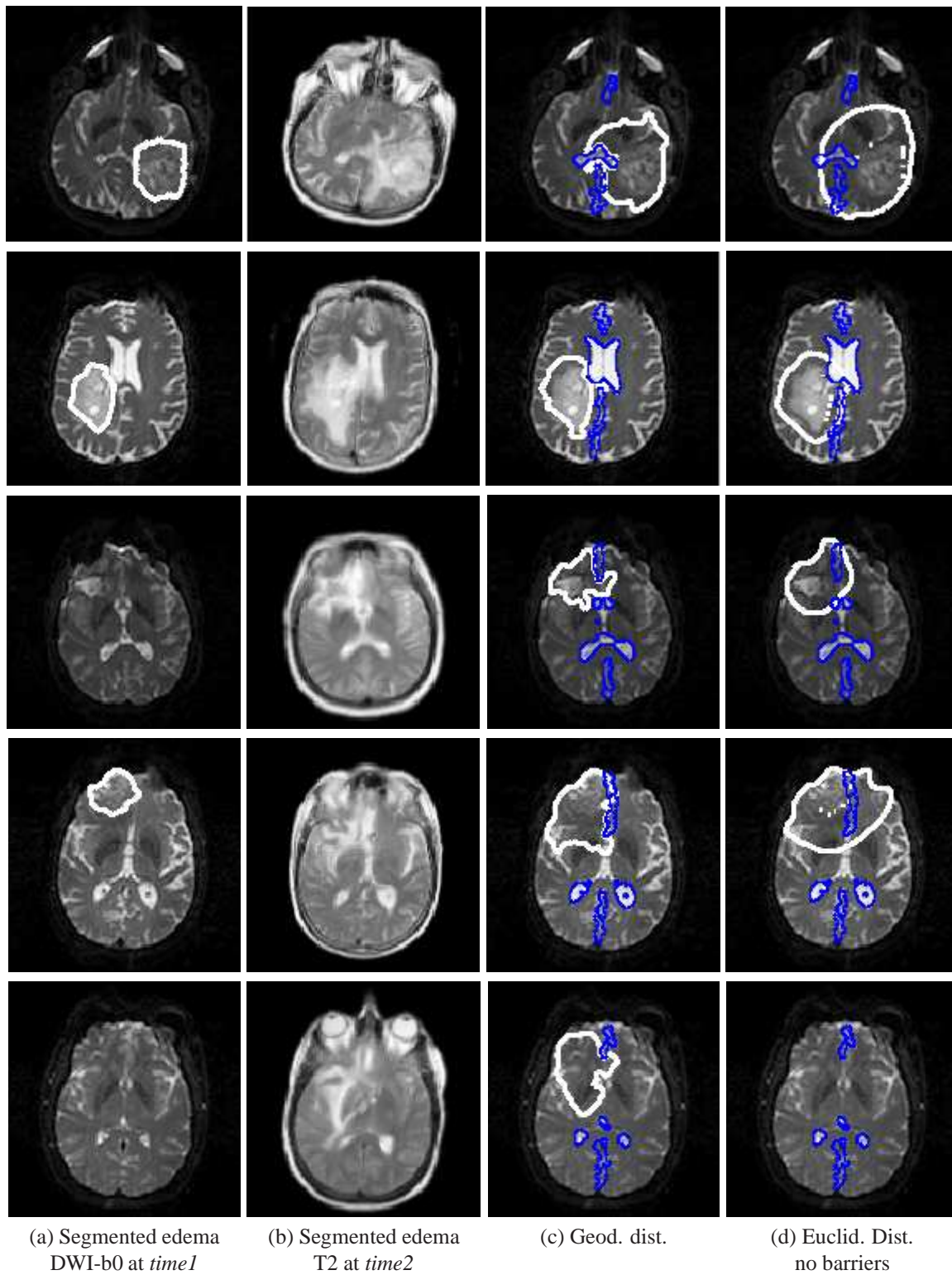| (a) Segmented edema DWI-b0 at *time1* | (b) Segmented edema T2 at *time2* | (c) Geod. dist. | (d) Euclid. Dist. no barriers |

Figure 6: Comparative results for 5 different patients of (c) geodesic and (d) Euclidean distance as used clinically (no barriers) models initiated from (a) segmented tumor at *time1* and (b) linearly registered followed up scans at *time2* (MRI-T2 or DWI). Barriers are shown in blue. As presented slices are part of a 3D volume, initial tumor contour in (a) is not present in two of the slices (row 3 and 5). This means that initial the tumor has not reached that slice but it will later grow there. Notice how in the example from the last row the Euclidean distance (d) has not reached the showed tumor location (b) while the geodesic distance (c) correctly shows the growth.

(a) Segmented edema
FLAIR *time2*

(b) Geod. dist.
FLAIR *time1*

(c) Euclid. Dist.
FLAIR *time1*

(d) Euclid. Dist.
with no barriers
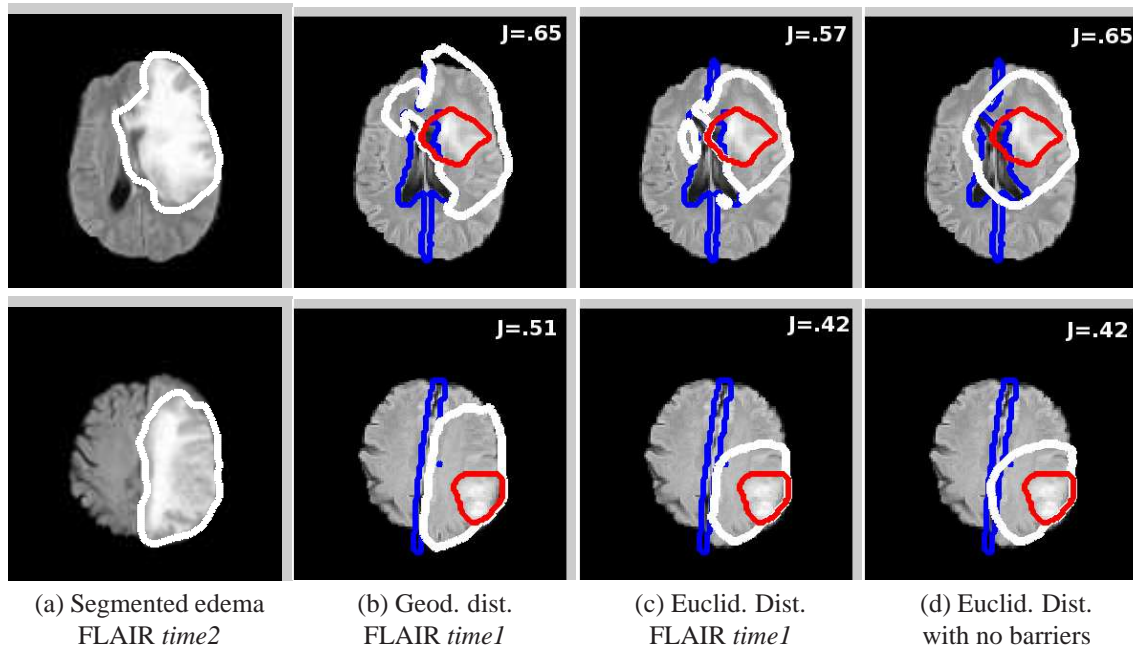
Figure 7: Comparative results for 2 patients showing: (a) manual edema segmentation on registered FLAIR *time1* (b) geodesic distance, (c) Euclidean distance with barriers and (d) Euclidean distance with no barriers on *time1* FLAIR. Barriers are shown in blue and *time1* edema segmentation used to initialize all distances in red. Jaccard scores between (b-d) distances and (a) *time2* segmentation are shown in white in the top right corner. Even though Jaccard scores are higher when no barriers are used for Euclidean segmentation (d), visual comparison shows that considering barriers (c) gives a better distance approximation of the real growth. The geodesic distance gives best overall results.

distance has not reached the particular tumor slice while the geodesic distance correctly models the growth.

Figure 7 shows sample comparative results between the two Euclidean cases (with and without barriers) and the geodesic distance.

To provide numerical comparison, we calculated the Jaccard (overlap) scores as shown in Table 2 for the three cases (geodesic versus two Euclidean methods). Numerical results show an average Jaccard score improvement of 5% and up to 20% on our datasets for simulated growth using the geodesic distance compared to the Euclidean distance (both in presence of barriers). For the Euclidean case that does not consider barriers, although the Jaccard scores are higher, but, as visual results in Figures 6 and 7 show, the calculated distances do not properly match the approximation of the real growth. The geodesic distance gives best overall results.

3.4.2. Comparison with an isotropic diffusion distance
3.4.3. Comparison of Different Tensor Extraction Methods
4. Discussion and Future Work

This study focuses on defining the correct margin of tumor occult cells that need to receive radiation therapy. This helps to control glioma tumors more effectively. Based on the fact that tumor cells diffuse in the same direction as water molecules, we used a geodesic distance model

| Patient | Geodesic dist. (%) | Jaccard score | |
		Euclidean dist. (%) with barriers	Euclidean dist. (%) no barriers
1	60	55	59
2	69	57	65
3	63	61	59
4	59	58	59
5	56	55	56
6	54	34	46
7	60	59	60
8	51	42	42
9	56	54	55
10	73	70	72
11	48	44	50
mean	59	53.54	56.63

Table 2: Jaccard (overlap) scores for comparing registered ground truth with Geodesic and Euclidean growth. $Jaccard(A, B) = (A \cap B)/(A \cup B)$

to locate the tumor invasion in the direction of water molecule motion. We evaluated our model on actual patient MRI and DTI data, which provide accurate and personalized information of white matter tracts, without requiring additional registration steps of diffusion tensors. Non of the previous models have been verified on a large set of patients with DTI data. We have hitherto tested our model on 11 dataset which were selected from our dataset of 64 patients. The access to this dataset enables us to be the first to test realistic diffusion-based invasion margin model on a large collection of patient DTIs. The visual comparison of our model with the conventional Euclidean distance method reveals that the anisotropic diffusion model can follow the tumor shape changes along the fibers better in time. The numerical results also indicate slight improvement.

Some issues that we think are of high priority to study in future work include:

- A problem with the available data is the low resolution of the data and the quality of data acquisition. The patients cannot tolerate the long period of the scan needed for clean data acquisition. Hence, the acquired data is rather noisy and of low quality, which increases the requirement of post processing. Figure 1 shows that the model can successfully track the clean tensors of the Atlas but results are somewhat less accurate for noisy clinical data.

-

- One of the necessities of the validation process is the segmentation of tumor and natural barriers. Therefore, we need at least five different structure segmentations (tumor in two time scans and three barriers) for each patient. This is a time-consuming task for the busy radio-anthologists. Despite the large amount of work done to automate the tumor segmentation process, there is no reliable segmentation software yet, especially for brains with abnormal regions (tumor). We expedited the process by using the semi-automatic tool proposed in [31]. However, we believe that automatically segmenting the barriers is not as difficult as the tumor, and it can save a considerable amount of time and effort. Automatically segmenting barriers from the available MRI and DWI data is another future work.

(a) Edema at *time2* (b) DTI-base diffusion distance (c) isotropic diffusion distance (d) Euclidean distance
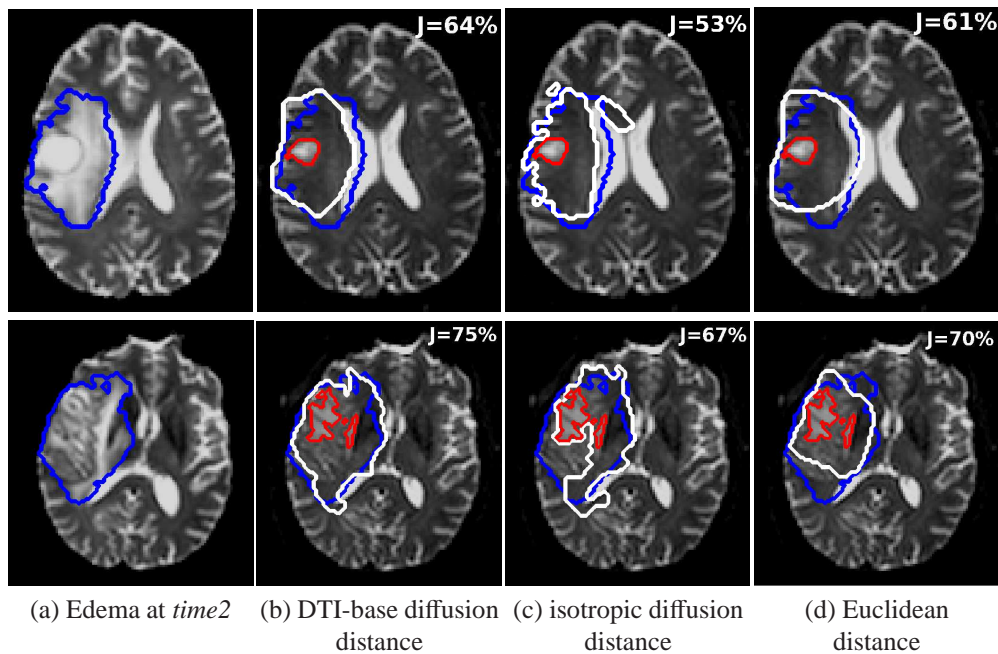
Figure 8: Motivation for the use of real DTI tensors. Comparison between (b) DTI-based anisotropic diffusion distance, (c) isotropic diffusion distance generated using synthetic isotropic tensors with different scales in WM and GM and the (d) Euclidean (uniform) distance. (a) shows the manual segmentation of edema at *time2* used as reference (ground truth) for comparison. Blue contours show this ground truth segmentation and red contours show corresponding distances. Distances (shown on *time1* data) are initiated from segmentation on *time1* and computed the same way as described in Section 3.1 (using the volume difference between *time2* and *time1* to identify corresponding isocontours). Jaccard scores are shown in white in the top right corner.

- A main source of error in the validation procedure is caused by the approximate registration of several time scans of patient data. Deriving a registration method that explicitly models the tumor mass effect can therefore improve the validation system. A proposed registration technique in the presence of mass effect incorporates a mechanical model into the registration (similar to [34], [35]).

- As shown by Painter [36], anisotropic diffusion might not be the optimal mathematical formulation of the cell migration process, which can be better modeled using a transport equation. Developing new mathematical models that use the full potential of DTI imaging, instead of the current reaction-diffusion based models, can increase the accuracy of tumor geometry and treatment margin prediction.

5. Conclusion

In this paper, we introduced the use of a geodesic distance on the Riemannian manifold of brain fibers, to detect the glioma brain tumor invasion margin. The model was tested on several real patients' data and a DTI atlas. In contrast to most of the previous works in this area which use registered tensors of the atlas, we used real tensors of the patients obtained from the standard

Patient	Jaccard score		
	Linear (%)	*Square (%)*	*Jbabdi. (%)*
1	60	33	60
2	69	27	65
3	63	43	62
4	59	59	57
5	56	49	54
6	54	14	54
7	60	62	60
8	51	23	49
9	56	52	55
10	73	71	72
11	48	33	50
mean	59	42.36	58

Table 3: Jaccard scores for comparing registered ground truth with Geodesic model using different tensor extraction methods.

clinical procedure. Comparative results between real growth in follow up scans and simulated growth based on geodesic distance and Euclidean distance prove that the use of the geodesic distance could significantly improve radiation therapy treatment. The geodesic distance obtained by our method can directly replace the Euclidean distance in the radiation therapy software and tools. State of the art radiation technologies enable very delicate radiation treatments in the scale of millimeters. Therefore, the complicated 3D shape obtained with the geodesic model can be used in the treatment planning.

Appendix A. Details on numerical aspects of the geodesic distance Hamilton-Jacobi equation

Numerical methods used for solving PDEs must be stable. This is important in medical applications where not considering stability issues of numerical methods can cause incorrect judgments of medical doctors which can lead to incorrect treatment methods. To support our statement, we use a visual example. Figure A.9 compares the result of applying two different numerical methods for solving the same PDE. Both methods are applied to the second order anisotropic parabolic diffusion equation of type 1 to solve the tumor growth model. In the image, the red contour shows the initial tumor area and, blue contours show the result of growth after a certain time. The left image shows the result of applying an unstable discretization method which results in an inhomogeneous contour [19], while the homogeneous right contour shows the result of a stable method [26]. More details on this analysis are given in [26].

In our study that we use full diffusion tensors, we are dealing with nonlinear PDEs rather than the simple linear ones. The stability of a finite difference solution to a nonlinear PDE cannot be guaranteed only by adjusting temporal or spatial resolutions. The method should meet certain criteria to be stable. Weickert [27] gives details about the criteria for solving a nonlinear anisotropic diffusion equation in the 2D case. Obtaining stable solution to a nonlinear PDE is even more difficult for the 3D case. Some prior works have used full diffusion tensors without considering stability issues of their numerical solution, [19] as an example. This results in an incorrect solution. We hereby prove that our used numerical method is stable:
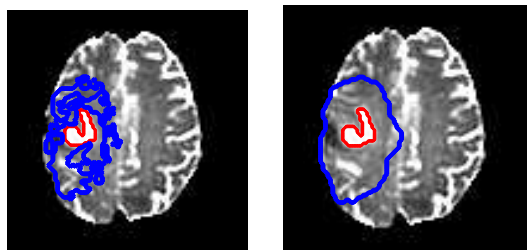
Figure A.9: Test of different discretization methods on anisotropic diffusion equation using real DTI data of patients with glioma. Red contour shows the starting area of the growth simulation. Left: Result of applying an unstable method, the blue contours show the result of an inhomogeneous growth caused by this method. Right: Result of applying a stable method which results in homogeneous contours.

The geodesic distance calculation results in solving a first order hyperbolic Hamilton Jacobi equation of the form $\psi_t + H(\psi_x) = 0$:

$$\begin{cases} \psi_t + |\text{grad}\psi| = 0 & \forall t > 0 \\ \psi(x, 0) = \psi_0(x) \end{cases} \tag{A.1}$$

where ψ is a levelset representation of the distance function and the the continuous flux $|\text{grad}\psi|^2$ is discretized as shown in Equation 16. We next discuss the consistency and stability of our finite difference-based solution for the geodesic distance equation.

Appendix A.1. Consistency

Consistency is achieved by applying the discretization in the direction of the wave motion (it depends on the sign of the velocity). Generally, upwind methods approximate derivatives by biasing the finite difference stencil in the direction where the characteristic information is coming. The upwind method guarantees a consistent finite difference scheme. The combination of the Euler differencing method with the upwind difference scheme gives a *consistent* finite difference scheme to the linear first order wave equation. But, Equation 15 is a non-linear equation of the general form $f(u) = u^2$. Engquist-Osher introduced the upwind method for nonlinear functions [37]. The numerical flux to the positive speed function f is defined as:

$$f(u) = \left((\max(D_x^- u, 0))^2 + (\min(D_x^+ u, 0))^2\right) \quad , \quad u = \psi_x \tag{A.2}$$

Consistency of this discretization scheme is proved in [37]. This method is extended to 3D in [38] for the quadratic Hamilton equation as defined in Equation 16.

Appendix A.2. Stability

A numerical method is said to be stable if small perturbations do not cause the resulting numerical solution to diverge without bound [39]. According to [30], stability guaranties that small errors are not amplified in time. For a first order hyperbolic equation, stability is achieved by forcing Courant-Friedrichs-Lewy condition (CLF condition), which states that numerical waves should propagate at least as fast as the physical wave. This means that the speed of the numerical wave $\frac{\Delta x}{\Delta t}$ must be at least as large as the physical wave speed $|u|$. The CLF condition for the Hamilton-Jacobi equation $\psi_t + H(\psi_x) = 0$ is given in [30] as

$$\Delta t \left(\frac{|H_1|}{\Delta x} + \frac{|H_2|}{\Delta y} + \frac{|H_3|}{\Delta z}\right) < 1 \tag{A.3}$$

where H_1, H_2 and H_3 are the spatial derivatives of H with respect to ψ_x, ψ_y and ψ_z, respectively. Using this scheme, it is easy to find the CLF condition for Geodesic distance Hamilton-Jacobi equation with nonlinear part

$$H(\phi) = \left|\text{grad}\psi\right|^2 = \sum_{k=1}^{3} \sum_{l=1}^{3} \frac{\partial \psi}{\partial x_l} \frac{\partial \psi}{\partial x_k} g^{kl} \tag{A.4}$$

where g^{kl} are the elements of the diffusion tensor. It is easy to see that

$$H_1 = \frac{\partial \psi}{\partial x_1} g^{11} + \frac{\partial \psi}{\partial x_2} g^{12} + \frac{\partial \psi}{\partial x_3} g^{13} \tag{A.5}$$

H_2 and H_3 are computed in the same way.

To conclude, we have shown that the finite difference method of Equation 16 used for solving the Hamilton-Jacobi equation is stable in space and its time stability is simply satisfied by choosing an appropriate time step.

References

[1] L. D. Lunsford, A. J. Martinez, R. E. Latchaw, Magnetic resonance imaging does not define tumor boundaries, Acta Radiol 369 (1986) 154 – 156.
[2] F. Hochberg, B. Slotnick, Neuropsychologic impairment in astxocytoma survivors, Neurology 30 (1980) 907–911.
[3] T. Kuroiwa, M. Ueki, Q. Chen, H. Suemasu, I. Taniguchi, R. Okeda, Biomechanical characteristics of brain edema: the difference between vasogenic-type and cytotoxic-type edema, Acta Neurochir Suppl 60 (1994) 158–61.
[4] L. Preziozi, Cancer modelling and simulation, Chapman & Hall, CRC Mathematical Biology and Medicine Series, 2003.
[5] J. Murray, Mathematical Biology, Springer-Verlag, Heidelberg, 1989.
[6] E.Konukoglu, Modeling Glioma Growth and Personalizing Growth Models in Medical Images, PhD Thesis, Universite Nice Sophia-Antipolis, 2009.
[7] A. Mohamed, C. Davatzikos, Finite element modeling of brain tumor mass-effect from 3d medical images, in: MICCAI, 2005, pp. 400–408.
[8] C. Hogea, F. Abraham, G. Biros, C. Davatzikos, A framework for soft tissue simulations with applications to modeling brain tumor mass-effect in 3d images., in: MICCAI, 2006.
[9] C. Hogea, C. Davatzikos, G. Biros, Modeling glioma growth and mass effect in 3d MR images of the brain, in: MICCAI, 2007.
[10] C. Hogea, C. Davatzikos, G. Biros, An image-driven parameter estimation problem for a reaction-diffusion glioma growth model with mass effects, Journal of Mathematical Biology 56 (2008) 793–825.
[11] C. Hogea, C. Davatzikos, G. Biros, Brain-tumor interaction biophysical models for medical image registration, SIAM Journal of Scientific Computing 30 (6) (2008) 793–825.
[12] O. Clatz, M. Sermesant, P. Bondiau, H. Delingette, S. Warfield, G. Malandain, N. Ayache, Realistic simulation of the 3d growth of brain tumors in MR images coupling diffusion with mass effect, IEEE Transactions on Medical Imaging 24 (10) (2005) 1334–1346.
[13] G. Cruywagen, D. Woodward, P. Tracqui, G. Bartoo, J. Murray, E. Alvord, The modeling of diffusive tumours, J. Biol. Sys 3 (1995) 937–945.
[14] P. Tracqui, G. Cruywagen, D. Woodward, G. Bartoo, J. Murray, E. Alvord, A mathematical model of glioma growth: the effect of chemotherapy on spatio-temporal growth, Cell Prolif 28 (1995) 17–31.
[15] D. Woodward, J. Cook, P. Tracqui, G. Cruywagen, J. Murray, E. Alvord, A mathematical model of glioma growth: the effect of extent of surgical resection, Cell Prolif 29 (1996) 269–288.
[16] G. A., L. Kluwe, B. Laube, H. Meissner, M. Berens, M. Westphal, Migration of human glioma cells on myelin., Neurosurgery 38 (1996) 755–764.
[17] K. Swanson, E. Alvord, J. Murray, A quantitative model for differential motility of gliomas in grey and white matter., Cell Proliferation 33 (2000) 317–329.
[18] K. Swanson, E. Alvord, J. Murray, Virtual brain tumors (gliomas) enhance the reality of medical imaging and highlight inadequacies of current therapy, British Journal of Cancer 85 (2002) 14–18.

[19] S. Jbabdi, E. Mandonnet, H. Duffau, L. Capelle, K. Swanson, M. Pelegrini, R. Guillevin, H. Benali, Simulation of anisotropic growth of low-grade gliomas using diffusion tensor imaging, Magnetic Resonance in Medicine 54 (2005) 616–624.
[20] E. Konukoglu, O. Clatz, B. Menze, M.-A. Weber, B. Stieltjes, E. Mandonnet, H. Delingette, N. Ayache, Image guided personalization of reaction-diffusion type tumor growth models using modified anisotropic eikonal equations, IEEE Transactions on Medical Imaging 29 (2010) 77–95.
[21] E. Konukoglu, O. Clatz, P.-Y. Bondiau, H. Delingette, N. Ayache, Extrapolating glioma invasion margin in brain magnetic resonance images: Suggesting new irradiation margins, Medical Image Analysis 14 (2) (2010) 111–125.
[22] E. Konukoglu, O. Clatz, P. Bondiau, H. Delingette, N. Ayache, Extrapolating tumor invasion margins for physiologically determined radiotherapy regions, in: MICCAI, 2006.
[23] D. Cobzas, P. Mosayebi, A. Murtha, M. Jagersand, Tumor invasion margin on the riemannian space of brain fibers, in: MICCAI, 2009.
[24] L. O'Donnell, S. Haker, C. Westin, New approaches to estimation of white matter connectivity in diffusion tensor MRI: Elliptic PDEs and geodesics in a tensor-warped space, in: MICCAI, 2002.
[25] C. Lenglet, R. Deriche, O. Faugeras, Inferring white matter geometry from diffusion tensor MRI: Applic. to connectivity mapping, in: MICCAI, 2004.
[26] P. Mosayebi, D. Cobzas, M. Jagersand, A. Murtha, Stability effects of finite difference methods on a mathematical tumor growth model, in: MMBIA at CVPR, 2010.
[27] J. Weickert, Anisotropic Diffusion in Image Processing, ECMI Series, Teubner-Verlag, Stuttgart, 1998.
[28] S. Osher, A level-set formulatin for the solution of the dirichlet problem for hamilton-jacobi equations., SIAM Journal of Mathematical Analysis 24 (5) (1993) 1145–1152.
[29] LONI, atlases http://www.loni.ucla.edu/atlases/.
[30] S. Osher, R. Fedkiwh, Level Set Methods and Dynamic Implicit Surfaces, Springer, New York, 2002.
[31] N. Birkbeck, D. Cobzas, M. Jagersand, A. Murtha, T. Kesztyues, An interactive graph-cut method for brain tumour segmentation, in: Workshop on Applications of Computer Vision (WACV), 2009.
[32] ExploreDTI, http://www.exploredti.com/.
[33] FSL, tools http://www.fmrib.ox.ac.uk/fsl/.
[34] A. Mohamed, E. Zacharaki, D. Shen, C. Davatzikos, Deformable registration of brain tumor images via a statistical model of tumor-induced deformation, Medical Image Analysis 10 (5) (2006) 752–763.
[35] A. Gooya, G. Biros, C. Davatzikos, An EM algorithm for brain tumor image registration: A tumor growth modeling based approach, in: MMBIA, 2010.
[36] K. Painter, Modelling cell migration strategies in the extracellular matrix, Journal of Mathematical Biology 58 (2009) 511–544.
[37] B. Engquist, S. Osher, One-sided difference approximations for nonlinear conservation laws., Mathematical Computing 36 (1981) 321–351.
[38] C. Lenglet, R. Deriche, O. Faugeras, Diffusion tensor magnetic resonance imaging brain connectivity mapping, in: TR INRIA, 2003.
[39] M. Heath, Scientific Computing, An Introductory Survey, McGraw-Hill, 2002.